J Mater Sci (2011) 46:7082–7089
DOI 10.1007/s10853-011-5555-z

SIZE DEPENDENT EFFECTS

Carbon-coated nano-sized $LiFe_{1-x}Mn_xPO_4$ solid solutions ($0 \leq x \leq 1$) obtained from phosphate–formate precursors

M. Yoncheva · V. Koleva · M. Mladenov · M. Sendova-Vassileva · M. Nikolaeva-Dimitrova · R. Stoyanova · E. Zhecheva

Received: 20 December 2010 / Accepted: 8 April 2011 / Published online: 22 April 2011

Abstract $LiFe_{1-x}Mn_xPO_4$ solid solutions in the whole concentration range ($0 \leq x \leq 1$) are obtained at 500 °C by a phosphate–formate precursor method. The method is based on the formation of homogeneous lithium–iron–manganese phosphate–formate precursors by freeze-drying of aqueous solutions containing Li(I), Fe(II), Mn(II), phosphate, and formate ions. Thermal treatment of the phosphate–formate precursors at temperatures at 500 °C yields nano-sized $LiFe_{1-x}Mn_xPO_4$ coated with carbon. The structure and the morphology of the $LiFe_{1-x}Mn_xPO_4$ compositions are studied by XRD, IR spectroscopy, and SEM analysis. The in situ formed carbon is analyzed by Raman spectroscopy. The electrochemical performance of $LiFe_{1-x}Mn_xPO_4$ is tested in model lithium cells using a galvanostatic mode. All $LiFe_{1-x}Mn_xPO_4$ compositions are characterized with an ordered olivine-type structure with a homogeneous Fe^{2+} and Mn^{2+} distribution in the 4*c* olivine sites. The morphology of $LiFe_{1-x}Mn_xPO_4$ consists of plate-like aggregates which are covered by in situ formed carbon. Inside the aggregates nano-sized isometric particles with narrow particles size distribution (between 60 and 100 nm) are visible. The structure of the deposited carbon presents a considerable disordered graphitic phase and does not depend on the Fe-to-Mn ratio. The solid solutions $LiFe_{1-x}Mn_xPO_4$ deliver a good reversible capacity due to the Fe^{2+}/Fe^{3+} and Mn^{2+}/Mn^{3+} redox-couples at 3.5 and 4.1 V, respectively.

M. Yoncheva · V. Koleva · R. Stoyanova · E. Zhecheva (✉)
Institute of General and Inorganic Chemistry,
Bulgarian Academy of Sciences, 1113 Sofia, Bulgaria
e-mail: zhecheva@svr.igic.bas.bg

M. Mladenov
Institute of Electrochemistry and Energy Sources,
Bulgarian Academy of Sciences, Sofia, Bulgaria

M. Sendova-Vassileva · M. Nikolaeva-Dimitrova
Central Laboratory of Solar Energy and New Energy Sources,
Bulgarian Academy of Sciences, Sofia, Bulgaria

Introduction

Phospho-olivines based on iron and manganese ($LiMPO_4$, M = Fe and Mn) are one of the most intensive studied during the last 10 years positive electrode materials for high-power lithium ion batteries [1]. The advantages of the phospho-olivines are their high cycling stability, excellent safety characteristics, and low cost. The iron analog $LiFePO_4$ displays a higher electrical conductivity and a better electrochemical performance as compared to the manganese analog $LiMnPO_4$. In addition, the delithiated $Li_{1-y}FePO_4$ is more stable than $Li_{1-y}MnPO_4$ and, consequently, more safer during storage [2, 3]. However, the chemical potential of the Mn^{2+}/Mn^{3+} redox-couple is higher than that of the Fe^{2+}/Fe^{3+} couple (4.1 vs. 3.4 V, respectively), as a result of which $LiMnPO_4$ has a higher energy density. The formation of solid solutions between $LiFePO_4$ and $LiMnPO_4$ opens new direction in the design of electrodes based on phospho-olivines with a potential application in HEV. Yamada et al. [4] have reported an improved electrochemical performance of $LiFe_{1-x}Mn_xPO_4$ with $x = 0{,}2$, 0.4, and 0.6, where the extraction and insertion of Li proceed at two steps at 3.4 and 4.1 V. Solid solutions $LiFe_{1-x}Mn_xPO_4$ have been prepared by solid state reactions at temperatures above 700 °C [5–7]. The sol–gel method was proved to be effective in the preparation of $LiFe_{1-x}Mn_xPO_4$ compositions [8, 9].

A characteristic feature of the phospho-olivines is the dependence of their electrochemical properties on the

method of synthesis. From an electrochemical point of view, the synthesis methods will be appropriate for electrode materials if they enable to obtain phospho-olivines with reduced particle dimensions being covered with in situ formed carbon. Recently, we have developed a new phosphate–formate precursor method for the preparation of nano-sized $LiFePO_4$ and $LiMnPO_4$ compositions [10, 11]. The method is based on the formation of homogeneous lithium–metal phosphate–formate precursors by freeze-drying of aqueous solutions containing Li(I), Fe(II) (or Mn(II)), phosphate, and formate ions. Thermal treatment of the phosphate–formate precursors at temperatures above 300 °C yields nanometric $LiFePO_4$ coated with carbon, while a higher temperature is needed for the preparation of pure $LiMnPO_4$ (450 °C). The advantage of this method is related to the ability to control the morphology of the phosphate–formate precursors by a simple variation of the concentration of the freeze-dried solutions. This, on its turn, has an impact on the carbon content, particle size distribution, and electrochemical properties of the target $LiFePO_4$ [12]. A new structural modification of $LiNiPO_4$ (with a Na_2CrO_4-type structure) has been prepared by this method [13]. The aptitude of the phosphate–formate precursor method to design simultaneously the precursors and the target product has also been demonstrated by the preparation of nano-crystalline cobalt and nickel phospho-olivines [14].

The aim of this contribution is to examine the applicability of the phosphate–formate precursor method for the preparation of solid solutions between $LiFePO_4$ and $LiMnPO_4$ in the whole concentration range. The structure and the morphology of the $LiFe_{1-x}Mn_xPO_4$ compositions are studied by XRD, IR spectroscopy, and SEM analysis. The in situ formed carbon is analyzed by Raman spectroscopy. The electrochemical performance of $LiFe_{1-x}Mn_xPO_4$ is tested in model lithium cells using a galvanostatic mode.

Experimental

The details of the synthesis of pure $LiFePO_4$ and $LiMnPO_4$ using the phosphate–formate precursor method are given elsewhere [10, 11]. We have adapted this method for the preparation of $LiFe_{1-x}Mn_xPO_4$ solid solutions. A transparent phosphate–formate solution of lithium, iron, and manganese was obtained by mixing $Fe(HCOO)_2{\cdot}2H_2O$, $Mn(HCOO)_2{\cdot}2H_2O$, and LiH_2PO_4. The concentration of solution is 0.05 M (with respect to the metal ions). The solution prepared at room temperature was frozen instantly with liquid nitrogen and dried in vacuum (20–30 mbars) at −20 °C with an Alpha-Christ Freeze-Dryer for about 18 h. The solid precursors were decomposed under flowing argon (99.999% purity) at 350 °C for 2 h. The solid products were further annealed at 500 for 10 h in an argon atmosphere. Special care is taken to eliminate any oxygen impurity in the Ar gas.

The content of M^{2+} in the starting $M(HCOO)_2{\cdot}2H_2O$ and prepared $LiFe_{1-x}Mn_xPO_4$ was determined complexometrically and the Li content—by atomic absorption analysis. Elemental analysis of C and H was performed using Elementar Analysensysteme GmbH (VarioEL analyser).

X-ray structural analysis was made by a Bruker Advance 8 diffractometer with Sol-X detector using Cu K_α radiation. Step-scan recordings for structure refinement by the Rietveld method were carried out using 0.02° 2θ steps of 10 s duration. The computer program FULLPROF was used in the calculations. The diffractometer point zero, the Lorentzian/Gaussian fraction of the pseudo-Voigt peak function, scale factor, the unit-cell parameters (a, b, and c), the thermal factor for the 4a, 4c, and 8d positions and the line half-width parameters were determined.

The IR spectra were recorded on a Fourier transform Nicolet Avatar-320 instrument using KBr pellets (resolution <2 cm^{-1}).

The Raman spectra were measured with a Horiba Jobin–Yvon LABRam HR800 spectrometer using the 600 l/mm grating and the 632.81 nm HeNe laser line for excitation. The samples were placed under the 100× achromatic objective of a BX41 microscope and measured in back scattering configuration. A neutral density filter was used to attenuate the laser radiation falling on the sample and it was 0.4 mW with a laser spot diameter of about 4 μm. Special care was taken that no heating effects are observable on the sample and in the spectra.

The morphology of the $LiFe_{1-x}Mn_xPO_4$ powders was observed by JEOL JSM-5510 scanning electron microscope.

The electrochemical charge–discharge of $LiFePO_4$ was carried out by using two-electrode cells of the type Li | $LiPF_6$ (EC:DMC) | $LiFePO_4$. The positive electrode, supported onto an aluminum foil, was a mixture containing 80% of the active composition $LiFePO_4$, 7.5% C-NERGY KS 6 L graphite (TIMCAL), 7.5% Super C65 (TIMCAL), and 5% polyvinylidene fluoride (PVDF). The electrolyte was 1 M $LiPF_6$ solution in ethylene carbonate and dimethyl carbonate (1:1 by volume) with less than 20 ppm of water. Lithium electrodes consisted of a clean lithium metal disk with diameter in 15 mm. The electrochemical reactions were carried out using an eight-channel Arbin BT2000 system in galvanostatic mode. The cells were mounted in a dry box under Ar atmosphere. For $LiFePO_4$, the cell is cycled between 4.4 and 2.2 V at C/20 rate. For $LiFe_{1-x}Mn_xPO_4$ ($x > 0$), the cells are charged up to 4.4 V at C/20 rate, keeping for 2.5 h at 4.4 V, followed by discharging to 2.2 V at C/20 rate.

Results and discussion

Structural and morphological characterization of $LiFe_{1-x}Mn_xPO_4$ solid solutions

At 500 °C, the phosphate–formate precursors yield pure mixed iron–manganese phospho-olivines. The XRD patterns of $LiFe_{1-x}Mn_xPO_4$ are compared in Fig. 1. All XRD patterns are indexed by a model comprising an ideal olivine structure with Li^+ in 4*a* and ($Fe^{2+}_{1-x}Mn^{2+}_x$) in 4*c* sites (space group *Pnma*). Recently it has been found that the $LiFe_{1-x}Mn_xPO_4$ compositions ($0 \leq x \leq 0.18$) obtained by sol–gel synthesis display the same extent of disorder of Mn^{2+} and Li^+ between the 4*a* and 4*c* sites [8]. Therefore, we have tested a possible Li and ($Fe_{0.5}Mn_{0.5}$) disorder between the 4*a* and 4*c* sites, but after the refinement the occupancy factors of Li at 4*a* and $Fe_{1/2}Mn_{1/2}$ at 4*c* tend to 1. This means that mixed $LiFe_{0.5}Mn_{0.5}PO_4$ composition without any Li-to-($Fe_{0.5}Mn_{0.5}$) disorder is formed from the phosphate–formate precursors at 500 °C. This is consistent with our data on the formation of defectless $LiFePO_4$ and $LiMnPO_4$ end compositions [10, 11]. This reveals that the phosphate–formate precursor method allows preparing lithium-transition metal phosphates with an ordered olivine-type structure.

The structural parameters of $LiFe_{1-x}Mn_xPO_4$ are given in Table 1. The substitution of Mn^{2+} for Fe^{2+} in the 4*c* positions causes a lattice expansion, which matches the ionic radii of Mn^{2+} and Fe^{2+}: 0.83 and 0.78 Å, respectively. In addition, after the progressive replacement of Fe^{2+} by Mn^{2+} there is a linear increase in the unit-cell parameters following the Vegard's law (Fig. 2). This reveals the formation of homogeneous solid solutions $LiFe_{1-x}Mn_xPO_4$ in the whole concentration range.

The formation of $LiFe_{1-x}Mn_xPO_4$ solid solutions is further studied by IR spectroscopy (Fig. 3). The assignment of the IR bands is based on the detailed IR studies of phospho-olivines [15–17]. The IR spectra of $LiFe_{1-x}Mn_xPO_4$ consist of well-resolved bands due to the characteristic vibrations of the PO_4^{3-} ion (Fig. 3): the ν_1 and ν_3 stretching modes appear in the region of 940–1150 cm^{-1}, while the bending $\nu_4(PO_4)$ mode is between 650 and 550 cm^{-1}. Both the symmetric ν_2 bending vibrations of PO_4^{3-} and the lithium-ion motions contribute to the bands in the region of 550–400 cm^{-1} [15, 16]. The nature of the transition metal ion affects mainly the stretching P–O vibrations, while the bending vibrations and the Li^+ motions remain insensitive. Using Tarte's assignment [15], the splitting of the ν_3 stretching P–O vibrations increases from the manganese to the iron member as follows: $\Delta\nu_3 = 1139 - 991 = 148\ cm^{-1}$ for $LiMnPO_4$ and $\Delta\nu_3 = 1139 - 970 = 169\ cm^{-1}$ for $LiFePO_4$. This means a larger deformation of the phosphate groups

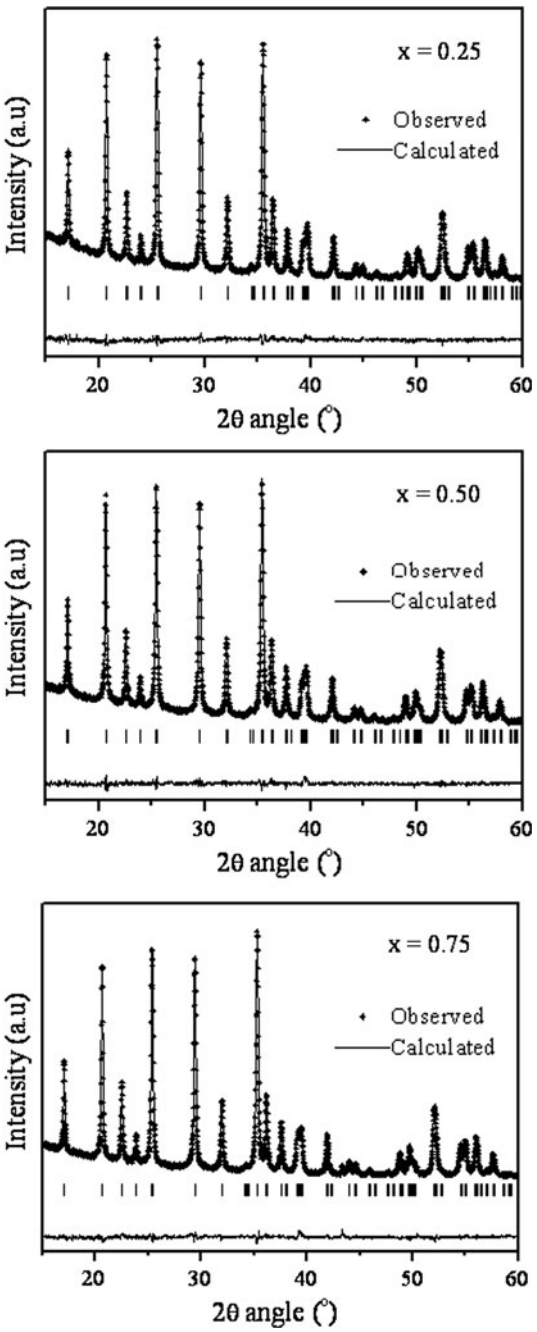

Fig. 1 Rietveld refinement of the XRD pattern of $LiFe_{1-x}Mn_xPO_4$

in $LiFePO_4$ in comparison with $LiMnPO_4$. In addition, the splitting can also be correlated with the ionization potential of transition metal ions: the $\Delta\nu_3$ value increases with increasing the ionization potential in the order $Mn^{2+} < Fe^{2+} < Co^{2+} < Ni^{2+}$ [15, 17]. For the intermediate $LiFe_{1-x}Mn_xPO_4$ compositions, the IR spectra in the region of the stretching P–O vibrations are a superposition of the IR spectrum of the two end analogs $LiFePO_4$ and $LiMnPO_4$. This reveals a two-mode behavior of the stretching P–O vibrations. From a spectroscopic point of

Table 1 Structural parameters of $LiFe_{1-x}Mn_xPO_4$ determined by Rietveld analysis

Atom	Site	x	y	z	B/Å^2	SOF[a]
$x = 0$						
$a = 10.3191(3)$, $b = 5.9985(1)$, $c = 4.6920(1)$, $V = 290.443(15)$Å^3						
$R_b = 3.70$, $R_f = 2.29$						
Li	4*a*	0	0	0	1.16	1
Fe	4*c*	0.2814(1)	1/4	0.9744(3)	0.65	1
P	4*c*	0.0953(2)	1/4	0.4213(4)	0.77	1
O1	4*c*	0.0962(5)	1/4	0.7395(7)	0.72	1
O2	4*c*	0.4560(5)	1/4	0.2151(6)	0.83	1
O3	8*d*	0.1656(3)	0.0493(5)	0.2850(5)	0.87	2
$x = 0.25$						
$a = 10.3563(2)$, $b = 6.0268(1)$, $c = 4.7056(1)$, $V = 293.706(13)$Å^3						
$R_b = 3.87$, $R_f = 2.07$						
Li	4*a*	0	0	0	1.00	1
Fe, Mn	4*c*	0.2822(1)	1/4	0.9724(3)	0.66	1
P	4*c*	0.0945(2)	1/4	0.4183(4)	0.74	1
O1	4*c*	0.0955(4)	1/4	0.7427(7)	0.36	1
O2	4*c*	0.4552(5)	1/4	0.2121(6)	0.79	1
O3	8*d*	0.1644(3)	0.0491(5)	0.2824(4)	0.59	2
$x = 0.50$						
$a = 10.3841(2)$, $b = 6.0501(1)$, $c = 4.7183(1)$, $V = 296.433(13)$Å^3						
$R_b = 2.66$, $R_f = 1.87$						
Li	4*a*	0	0	0	0.95	1
Fe, Mn	4*c*	0.2820(1)	1/4	0.9722(2)	0.73	1
P	4*c*	0.0944(1)	1/4	0.4164(3)	0.66	1
O1	4*c*	0.0952(4)	1/4	0.7396(6)	0.42	1
O2	4*c*	0.4571(4)	1/4	0.2135(6)	0.60	1
O3	8*d*	0.1635(3)	0.0504(4)	0.2816(4)	0.51	2
$x = 0.75$						
$a = 10.4158(2)$, $b = 6.0762(1)$, $c = 4.7314(1)$, $V = 299.450(12)$Å^3						
$R_b = 3.05$, $R_f = 2.07$						
Li	4*a*	0	0	0	0.85	1
Fe, Mn	4*c*	0.2819(1)	1/4	0.9709(2)	0.68	1
P	4*c*	0.0939(1)	1/4	0.4142(3)	0.80	1
O1	4*c*	0.0949(4)	1/4	0.7334(7)	0.58	1
O2	4*c*	0.4572(4)	1/4	0.2149(5)	0.62	1
O3	8*d*	0.1625(3)	0.0520(4)	0.2791(4)	0.44	2
$x = 1$						
$a = 10.4376(2)$, $b = 6.0956(1)$, $c = 4.7425(1)$, $V = 301.744(12)$Å^3						
$R_b = 2.50$, $R_f = 1.88$						
Li	4*a*	0	0	0	1.22	1
Mn	4*c*	0.2815(1)	1/4	0.9704(3)	0.63	1
P	4*c*	0.0934(2)	1/4	0.4109(4)	0.74	1
O1	4*c*	0.0967(4)	1/4	0.7287(7)	0.36	1
O2	4*c*	0.4573(4)	1/4	0.2133(7)	0.79	1
O3	8*d*	0.1621(3)	0.0513(5)	0.2766(5)	0.59	2

[a] The site occupation factor (SOF) is given as number of atoms per formula unit

view, the two-mode behavior is not an unusual feature for mixed crystals based on isomorphous substitution [18]. Therefore, the observation of a two-mode behavior of the $LiFe_{1-x}Mn_xPO_4$ solid solutions does not contradict to a homogeneous distribution of Fe^{2+} and Mn^{2+} on the 4*c* positions. In addition, a two-mode behavior has also been established by Frech et al. [19] for the $LiFe_{1-x}Mn_xPO_4$ composition with $x = 0.5$.

A characteristic feature of the phosphate–formate precursor method is the deposition of carbon during the decomposition of formic acid [10]. Based on XPS studies, it has been shown that the carbon is mainly deposited on the particle surface, thus preventing the particle growth at temperatures lower than 600 °C [10]. For the intermediate compositions $LiFe_{1-x}Mn_xPO_4$, the total amount of the in situ formed carbon varies between 1.6 and 2.3 wt%: 2.3 wt% for $LiFePO_4$, 2.1 wt% $LiFe_{0.5}Mn_{0.5}PO_4$, and 1.6 wt% for $LiMnPO_4$. It appears that total amount of the in situ formed carbon is slightly dependent on the iron-to-manganese ratio with a tendency to decrease for the $LiMnPO_4$ analog. This can be understood if we take into account the mechanism of the decomposition of the metal formates. It has been shown that the in situ formed carbon originates mainly from the evolving CO, which further disproportionates into CO_2 and carbon ($2CO \leftrightarrow CO_2 + C$, Boudouard's reaction) [20–22]. For the mixed iron–manganese precursors, it seems that the type of the transition metal ion (Fe^{2+} or Mn^{2+}) affects slightly the CO disproportionation reaction.

To analyze the structure of the in situ formed carbon, Raman spectroscopy measurements were undertaken. Figure 4 shows the typical Raman spectra in the region of the carbon bands of $LiFe_{1-x}Mn_xPO4$ with $x = 0$, 0.5, and 1. The spectra are dominated by two intensive bands at 1345 and 1590 cm^{-1}. These two bands are defined as D (disorder) and G (graphite) peaks and are fingerprints of disordered carbon with graphite like medium-range order [23–25]. The G peak is due to the bond stretching of all pairs of sp^2 atoms in both rings and chains, and the D peak is due to the breathing modes of the sp^2 rings and is associated with the breakage of the symmetry at the edges of graphite sheets [26, 27]. The higher the I_D/I_G intensity ratio is and the broader the D peak is, the more disordered is the graphitic phase [23, 24]. This is what we observe for all $LiFe_{1-x}Mn_xPO_4$ compositions: the I_D/I_G intensity ratio is about 5 and the line width of the D peak is about 80 cm^{-1}. The well resolved G and D bands, as well as the intensity and broad shape of the D band, indicate a considerable disorder in the graphitic phase formed at 500 °C on $LiFe_{1-x}Mn_xPO_4$ during the formate decomposition reaction. In addition to the G and D bands, two broad peaks at 1220 and 1475 cm^{-1} can be resolved (Fig. 4). The origin of these Raman bands is not clear.

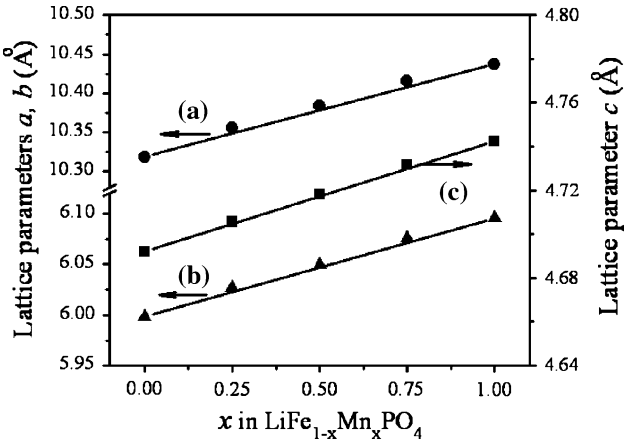

Fig. 2 Lattice parameters of $LiFe_{1-x}Mn_xPO_4$

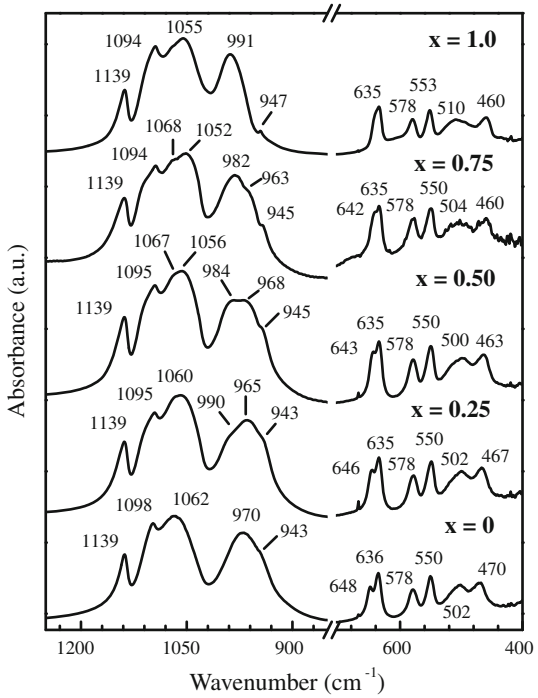

Fig. 3 IR spectra of $LiFe_{1-x}Mn_xPO_4$

However, additional peaks are also observed for amorphous carbon materials derived from decomposition of citric acid [28], glycolic acid [29], cellulose [30], sucrose [31], ferrocene, and pyromellitic acid [32]. Therefore, the direct comparison and the fitting with two and four bands lead to the conclusion that the Raman spectra of the carbon on the surface of the $LiFe_{1-x}Mn_xPO_4$ samples do not depend on the Fe-to-Mn ratio.

In addition, the symmetric ν_1 stretching mode of PO_4^{3-} appears as a very weak band at 947 cm^{-1} and the ν_3 mode is even not observed. This fact evidences once again that the carbon is deposited on the particle surface, thus screening the signal from the PO_4^{3-} groups.

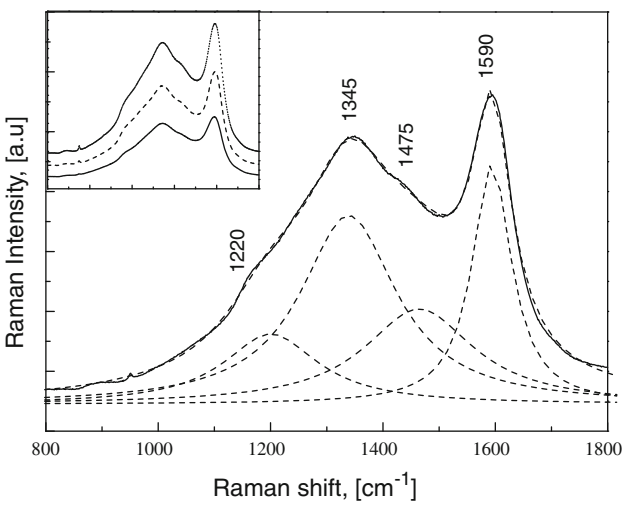

Fig. 4 Typical Raman spectrum of $LiFe_{0.5}Mn_{0.5}PO_4$ in the region of the carbon bands fitted with four Lorentzian peaks. The *inset* shows the Raman spectra for $LiMnPO_4$ (*solid line*), $LiFe_{0.5}Mn_{0.5}PO_4$ (*dashed line*) and $LiFePO_4$ (*dotted line*) in the same wavenumber range

An advantage of the phosphate–formate precursor method is the ability to control the particle size dimensions by a simple variation of the concentration of the solutions subjected to freeze-drying. Precursors obtained from diluted solutions are more suitable for the preparation of nano-sized $LiFePO_4$ and $LiMnPO_4$ olivines [10, 11]. Therefore, the mixed iron–manganese precursors prepared by freeze-drying are obtained from diluted solutions (0.05 M). The SEM images of $LiFe_{1-x}Mn_xPO_4$ ($x = 0$, 0.5, and 1) derived at 500 °C from the corresponding precursors are shown in Fig. 5. The morphology of all phospho-olivines comprises plate-like aggregates with micrometric dimensions (Fig. 5). The surface of the aggregates is smooth and, due to the carbon coating, the individual particles are not observed. When breaking the aggregates, nearly isometric particles with sizes varying between 60 and 120 nm become visible. The mean particle size is only slightly dependent on the Mn content: 85 ±15 nm for $LiFePO_4$, 70 ± 10 nm for $LiFe_{1-x}Mn_xPO_4$, and 90 ± 15 nm for $LiMnPO_4$. The particle size distribution is more sensitive toward the Mn content (Fig. 5). The narrowest particle size distribution is observed for the mixed $LiFe_{1-x}Mn_xPO_4$ olivines: about 60% of particles have dimensions in the range of 60–80 nm. The end compositions $LiFePO_4$ and $LiMnPO_4$ exhibit a slightly broader particles size distribution where about 90% of the particles are between 60 and 120 nm (Fig. 5).

The particle size and the carbon content have been shown to affect the electrochemical performance of the phospho-olivines. For a particle distributed in the

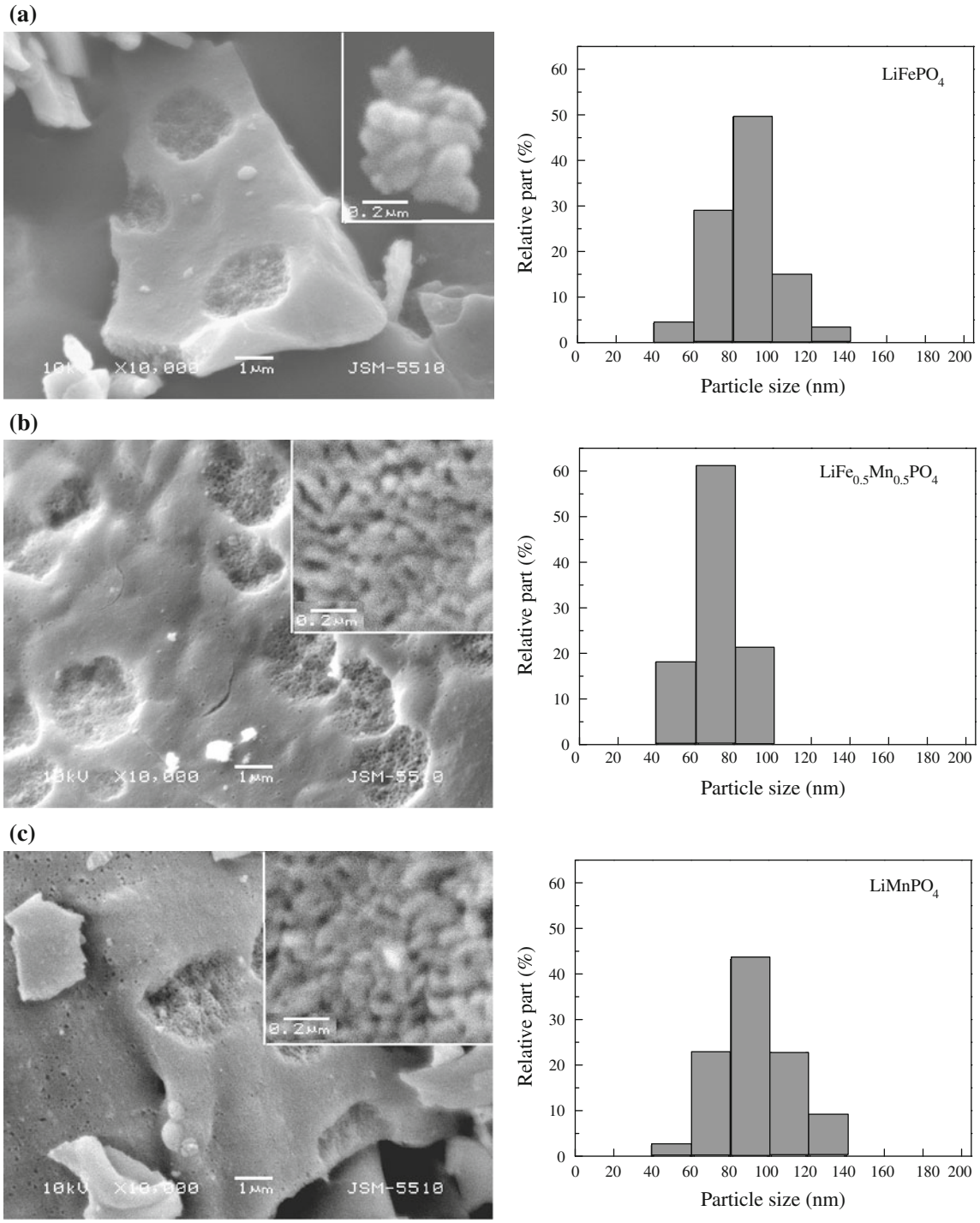

Fig. 5 SEM images and particle size distribution of $LiFePO_4$ (**a**), $LiFe_{0.5}Mn_{0.5}PO_4$ (**b**), and $LiMnPO_4$ (**c**). The *inset* indicates the SEM images at higher magnification

nanometric region (<100 nm), Van der Ven et al. [33] have demonstrated that the flat voltage profile is transformed in a way that mimics the sloping voltage profile similarly to that of a solid solution. The role of the in situ formed carbon is to make the penetration of the electrolyte into the cathode material easily [28]. For $LiFePO_4$, we have established that the particle size distribution affects the voltage profile, while the specific capacity is mainly dependent on the carbon content deposited on the particle surfaces [12]. The highest capacity and the best capacity retention are observed for ordered $LiFePO_4$ obtained at 500 °C which is

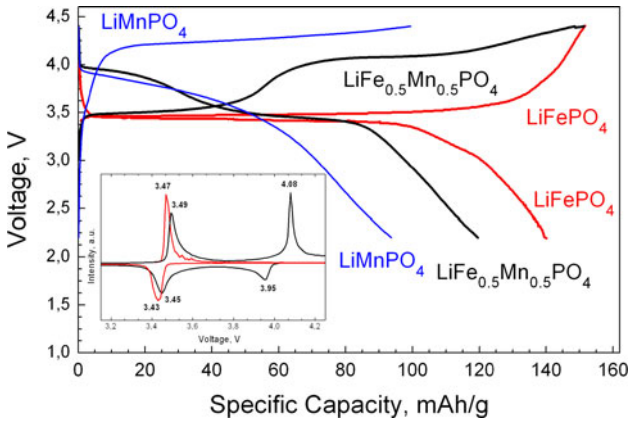

Fig. 6 First charge/discharge curves of $LiFePO_4$ (*red lines*), $LiFe_{0.5}Mn_{0.5}PO_4$ (*black lines*), and LiMnPO4 (*blue lines*). The *inset* corresponds to the derivative of the charge/discharge curves (Color figure online)

characterized by low particle dimensions (about 85 nm), a narrow particle size distribution and a carbon content of about 2.3 mass% [12].

Since the $LiFe_{1-x}Mn_xPO_4$ solid solutions display nanometric particles with close particle size distribution and a similar carbon content, it is now possible to examine the effect of the Mn^{2+} ions on the electrochemical extraction and insertion of Li^+. Figure 6 compares the first charge/discharge curves of $LiFe_{1-x}Mn_xPO_4$ with $x = 0$, 0.5, and 1. As one expected, nano-sized $LiFe_{1-x}Mn_xPO_4$ olivines deliver a good reversible capacity, reaching 140 mAh/g. For $LiFePO_4$, the main oxidation and reduction peaks corresponding to the Fe^{2+}/Fe^{3+} redox couple appear at 3.47 and 3.43 V, respectively, while the Mn^{2+}/Mn^{3+} redox couple for $LiMnPO_4$ operates at higher potential: at 4.2 and 3.9 V, respectively. The comparison shows clearly that the cell polarization is significant for $LiMnPO_4$, as a result of which the discharge capacity corresponding to Mn^{3+}/Mn^{2+} couple is reduced from 140 mAh/g for $LiFePO_4$ to 95 mAh/g for $LiMnPO_4$. This is consistent with the lower electronic conductivity of $LiMnPO_4$ [34]. For $LiFe_{0.5}Mn_{0.5}PO_4$, the voltage profile is a superposition of potentials of the redox Fe^{2+}/Fe^{3+} and Mn^{2+}/Mn^{3+} couples: 3.49/3.45 and 4.08/3.95 V, respectively. This reveals that the iron ions are reduced before the manganese ions, in good agreement with previous data [35]. It is important that the cell polarization in the region of the Mn^{2+}/Mn^{3+} couple is significantly reduced, thus allowing $LiFe_{0.5}Mn_{0.5}PO_4$ to deliver a higher discharge capacity: 120 mAh/g. An improved electrochemical performance of the mixed iron–manganese compositions in comparison with that of $LiMnPO_4$ has been established for $LiFe_{0.4}Mn_{0.6}PO_4$ by Nedoseykina et al. [36]. The good electrochemical performance of $LiFe_{0.5}Mn_{0.5}PO_4$ can be related with its perfect olivine structure. The Li^+ and Mn^{2+} disorder between the 4*a* and 4*c* olivine positions leads to a blockage of the one-dimensional lithium ion transport pathway, thus reducing the electrochemical activity of the $LiMnPO_4$ prepared at low temperatures [37].

Conclusions

$LiFe_{1-x}Mn_xPO_4$ solid solutions in the whole concentration range ($0 \leq x \leq 1$) are obtained at 500 °C by the phosphate–formate precursor method. All $LiFe_{1-x}Mn_xPO_4$ compositions are characterized with an ordered olivine-type structure, which does not have any Li-to-($Fe_{1-x}Mn_x$) disorder. The iron and manganese ions are homogeneously distributed at the 4*c* olivine sites. The morphology of $LiFe_{1-x}Mn_xPO_4$ consists of plate-like aggregates covered with in situ formed carbon. Inside the aggregates nano-sized isometric particles with a close particle size distribution (between 60 and 100 nm) are formed. The structure of the deposited carbon is defined as a considerably disordered graphitic phase and does not depend on the Fe-to-Mn ratio. $LiFe_{1-x}Mn_xPO_4$ solid solutions deliver a good reversible capacity due to the Fe^{2+}/Fe^{3+} and Mn^{2+}/Mn^{3+} redox-couples at 3.5 and 4.1 V, respectively. Although the voltage range and the electrolyte composition were not optimized, it seems that the $LiFe_{1-x}Mn_xPO_4$ compositions display a satisfactory reversible capacity in comparison with $LiFePO_4$. This reveals the advantages of the phosphate–formate precursor method for the preparation of single and mixed phospho-olivines.

Acknowledgements Authors are grateful to the financial support from the National Science Fund of Bulgaria (Ch1701/2007). Partial financial support by the National Centre for New Materials UNION (Contract No DCVP-02/2/2009) is also acknowledged. We are grateful of TIMCAL Company for providing carbon additives. The Raman equipment is used in the framework of project Integrated Research Centres at the Universities No DO02-167/2008.

References

1. Ellis BL, Lee KT, Nazar LF (2010) Chem Mater 22:1059
2. Ong SP, Jain A, Hautier G, Kang B, Ceder G (2010) Electrochem Commun 12:427
3. Chen G, Richardson TJ (2010) J Power Sources 195:1221
4. Yamada A, Chung S-C (2001) J Electrochem Soc 148:A960
5. Nakamura T, Sakumoto K, Okamoto M, Seki S, Kobayashi Y, Takeuchi T, Tabuchi M, Yamada Y (2007) J Power Sour 174:435
6. Molenda J, Ojczyk W, Marzec J (2007) J Power Sour 174:689
7. Kopec M, Yamada A, Kobayashi G, Nishimura S, Kanno R, Mauger A, Gendron F, Julien CM (2009) J Power Sour 189:1154
8. Bramnik NN, Bramnik KG, Nikolowski K, Hinterstein M, Baehtz C, Ehrenberg H (2005) Electrochem Solid State Lett 8:A379
9. Bini M, Mozzati MC, Galinetto P, Capsoni D, Ferrari S, Grandi MS, Massarotti V (2009) J Solid State Chem 182:1972
10. Koleva V, Zhecheva E, Stoyanova R (2009) J Alloys Compd 476:950
11. Koleva V, Stoyanova R, Zhecheva E (2009) Mater Chem Phys 121:370

12. Zhecheva E, Mladenov M, Zlatilova P, Koleva V, Stoyanova R (2010) J Phys Chem Solids 71:848
13. Koleva V, Stoyanova R, Zhecheva E (2010) Eur J Inorg Chem 127
14. Koleva V, Zhecheva E, Stoyanova R (2010) Eur J Inorg Chem 4091
15. Paques-Ledent MT, Tarte P (1972) Spectrochim Acta 29A:673
16. Burba C, Frech R (2006) Spectrochim Acta 65A:44
17. Ait Salah A, Jozwiak P, Zaghib K, Garbarczyk J, Gendron F, Manger A, Julien CM (2006) Spectrochim Acta 65A:1007
18. Tarte P, Rulmont A, Liégeois-Duyckaerts M, Cahay R, Winand JM (1991) Solid State Ionics 42:177
19. Burba C, Frech R (2007) J Power Sour 172:870
20. Meisel T, Halmos Z, Seybold K, Pungor E (1975) J Thermal Anal Calorim 7:73
21. Langbein H, Christen S, Bonsdorf G (1999) Thermochim Acta 327:173
22. Kenfack F, Langbein H (2005) Thermochim Acta 426:61
23. Liu Y, Pan C, Wang J (2004) J Mater Sci 39:1091. doi: 10.1023/B:JMSC.0000012952.20840.09
24. Tuinstra F, Koenig JL (1970) J Chem Phys 53:1126
25. Robertson J (2002) J Non Cryst Solids 299–302:798
26. Ferrari AC, Robertson J (2001) Phys Rev B64:075414
27. Ferrari AC, Robertson J (2001) Phys Rev B61:14095
28. Palomares V, Goni A, Gil de Muro I, Meatza I, Bengoechea M, Cantero I, Rojo T (2010) J Power Sour 195:7661
29. Doeff MM, Hu Y, McLarnon F, Kostecki R (2003) Electrochem Solid State Lett 6:A207
30. Maccario M, Croguennec L, Desbat B, Couzi M, Le Cras F, Servant L (2008) J Electrochem Soc 155:A879
31. Ait Salah A, Mauger A, Zaghib K, Goudenough JB, Ravet N, Gauthier M, Gendron F, Julien CM (2006) J Electrochem Soc 153:A1692
32. Doeff MM, Wilcox JD, Yu R, Aumentado A, Marcinek M, Kostecki R (2008) J Solid State Electrochem 12:995
33. Van der Ven A, Wagemaker M (2009) Electrochem Commun 11:881
34. Yamada A, Hosoya M, Chung S-C, Kudo Y, Hinokuma K, Liu KY, Nishi Y (2003) J Power Sour 119–121:232
35. Yamada A, Takei Y, Koizumi H, Sonoyama N, Kanno R, Itoh K, Yonemura M, Kamiyama T (2006) Chem Mater 18:804
36. Nedoseykina T, Kim MG, Park S-A, Kim H-S, Kim S-B, Cho J, Lee Y (2010) Electrochim Acta 55:8876
37. Fang H, Pan Z, Li L, Yang Y, Yan G, Li G, Wei S (2008) Electrochem Commun 10:1071